Contents lists available at ScienceDirect

Materials and Design

journal homepage: www.elsevier.com

Preparation and characterization of β-SiAlON/TiN nanocomposites sintered by spark plasma sintering and pressureless sintering

Kh. A. Nekouee, R. Azari Khosroshahi *

Faculty of Materials Engineering, Sahand University of Technology, Tabriz, Iran

ARTICLE INFO

Article history:
Received 28 June 2016
Received in revised form 24 September 2016
Accepted 26 September 2016
Available online xxx

Keywords:
β-SiAlON/TiN nanocomposites
Mechanical alloying
Sintering
Phase composition
Microstructure
Mechanical properties

ABSTRACT

In this research, β-SiAlON/TiN nanocomposites were synthesized from Si_3N_4, Al_2O_3, AlN and TiO_2 powders by the combination of mechanical alloying and the subsequent pressureless and spark plasma sintering. The effects of submicron and nanometer size TiO_2 precursors on the microstructure, phase composition and mechanical properties of the SiAlON composites were investigated. Majority of Si_3N_4 particles were transformed into nanometer size which were embedded in the amorphous phase. Spark plasma sintering of the β-SiAlON/TiN powder at temperatures as low as 1750 °C resulted in full density ceramics. In addition, it was observed that sintered bodies by pressureless sintering, had lower mechanical properties than the spark plasma sintered samples. Moreover, spark plasma sintered samples demonstrated optimal friction coefficient of 0.6.

1. Introduction

Ceramics of silicon nitride have gotten high temperature structural applications due to their high strength, good friction, oxidation properties, low density and high erosion and chemical corrosion resistance [1–3]. Furthermore, these ceramics have been employed in aerospace and automotive industry [1,4,5]. SiAlON is a general name for a big family of ceramic alloys based on silicon nitride. Following their discovery in 1970, they have been actively developed [4,6,7]. SiAlONs as a result of their good tribology and low friction coefficient properties and resistance to chemical corrosion can be employed in cutting tools, wire die extension and blast nozzles [1,8,9].

SiAlONs exist in a broad range of compositions which include several different families of crystal structures such as β, α, O and X-SiAlON [10]. β-SiAlON ($Si_{6-z}Al_zO_zN_{8-z}$) is one of the most important structures of SiAlON where, z varies from 0 (pure Si_3N_4) to 4.2 with hexagonal structure [10–12]. Each unit cell of β-SiAlON has been produced by two unit cell of silicon nitride [1,4,5].

SiAlON composites with other ceramics like TiN are suitable candidates for specific applications at ambient and high temperatures due to their high hardness, fracture toughness and good oxidation resistance [13–19]. Due to their good thermal shock, corrosion resistance and thermal and dimensional stability, they have extensively attracted the attention of many researchers [15,20–25].

High sintering temperature of SiAlON is a challenge for extending such material for industrial applications [10,22,26,27]. Improvement of the composition and microstructure properties can be achieved by carefully controlling the process parameters and methods [12,28–33]. Additionally, synthesis and fabrication methods involving liquid, solid state and gas pressure processing routes were developed in order to reduce the sintering temperature and fabrication costs [6,22,31,34–36].

Powders such as Si_3N_4, TiN, Ti, Al_2O_3 and AlN with different compositions can be synthesized by planetary ball milling to obtain SiAlON-TiN nanocomposites [10,22,27,37–39]. Available sintering techniques (from solid state routes) ranging from pressure less sintering (PLS) to gas pressure sintering (GPS) can be employed for the sintering of SiAlON and nanocomposites [6,40–42]. Furthermore, sintering techniques like spark plasma sintering (SPS) were developed as a rapid and effective sintering technique for densification of various materials like SiAlONs and its composites [25,30,37,43,44].

Ceramics like SiAlON and its nanocomposites with high performance can be obtained by producing liquid phases in their systems during their sintering [24]. By employing sintering additives e.g. Al_2O_3, TiO_2 and Y_2O_3, promotion of densification via the liquid phase sintering can occur [20,21,34,37]. By reacting Si_3N_4, AlN, Al_2O_3 and TiO_2 as starting materials; a low-viscosity liquid phase with some SiO_2 content will be formed, and as a result, grain boundary glasses will develop [45,46].

Important goal in the synthesis and manufacturing of SiAlONs and its composites is to achieve optimal mechanical properties by PLS and SPS processes [23,47]. Fabrication of SiAlON/TiN ceramics with low cost is achievable by using low cost combustion synthesized β-Si_3N_4 and TiO_2 powders with sintering at lower temperatures. Mandal et al. [22] have studied the PLS of β-SiAlON from low cost

* Corresponding author.
Email address: rakhosroshahi@Gmail.com (R.Azari Khosroshahi)

http://dx.doi.org/10.1016/j.matdes.2016.09.090
0264-1275/

combustion synthesized Si_3N_4 powders, although, SPS of SiAlON and PLS or SPS of its composites with TiN have not been reported. Therefore; the aim of this study was to evaluate and compare the results of the PLS and SPS processes to achieve SiAlON/TiN nanocomposites by mechanical alloying of low cost precursors with nanometer and submicron sizes of TiO_2 additive powders. This study has two sections. Properties of mechanically activated powders are discussed in the first section, and physical and mechanical properties of the bulk samples are evaluated at the second section.

2. Experimental

2.1. Sample preparation

Samples were prepared from High-purity (˃99 wt.%) powders according to Table 1. Si_3N_4 (β-Si_3N_4 composition, − 325 mesh powder size), AlN (powder size: < 10 μm (micron)), two batches of TiO_2 (powder size: Nanometer and submicron powder) and Al_2O_3 (powder size: < 50 nm) were selected as starting materials for synthesizing SiAlON(z = 1.5)/TiN nanocomposites. Si_3N_4 powders were obtained from Beijing Chanlian-Dacheng Trade Co., China and other powders were purchased from Sigma-Aldrich company products.

The mentioned precursors (acronyms to SB0, SBM0 (composite with submicronized TiO_2) and SBN0 (composite with nanometer size TiO_2)) were mechanical milled in a poly amid jar in isopropanol alcohol atmosphere filled with High-purity argon gas using Al_2O_3 balls as milling agent and media respectively. The milling of precursors for 5 h (acronyms to SB50, SBM50 and SBN50) and 10 h (acronyms to SB100, SBM100 and SBN100) were executed by planetary ball mill (PM2400, 400 rpm). The ball-to-powder weight ratio of 10:1 was employed. The granulated powder mixtures were sieved by a 150 micrometer mesh and then pressed in 20 MPa hydraulic die after the addition of 1 wt.% PVB as binder into pellets of 25 mm in diameter and 7–8 mm in thickness. Finally, the pellets were pressed under 200 MPa of cold iso static press. The pressed pellets were fired in an electrical furnace. Afterwards, the pellets were heated at a heating rate of 5 °C min^{-1} and then for slowly burning out the binder they dwelled at 600 °C for 30 min. Then, they were heated at temperatures of 1750 °C for 90 min (acronyms to SBpls75, SBMpls75 and SBNpls75) in a pressureless atmosphere filled with nitrogen gas. At this point, the well mechanically alloyed powders were maintained at 1750 °C for 12 min under a pressure of 30 MPa (from here onwards, the samples prepared under the SPS conditions will be acronyms to SBsps75, SBMsps75, SBNsps75) in a vacuum condition by SPS machine (Nanozint 10).

In order to restrain and prevent sticking of powders to die during spark plasma sintering, graphite foils were employed. Heating rate of 30 °C min^{-1} of capsulated powders in SPS sintering technique was selected. The set-up allows a cooling rate of ˃200 °C min^{-1} in the temperature range up to 100 °C min^{-1}.

Table 1
Composition (weight percent) of different SiAlON/TiN composites.

Sample	S_3N_4	Al_2O_3	AlN	TiO_2	Predicted TiN
SB	Rest	15.56	9.33	0	0
SBM	Rest	15.56	9.33	15 (micronized)	13
SBN	Rest	15.56	9.33	15 (nano-sized)	13

2.2. Characterization technique

The particle size of the powders, distribution of the elements and microstructure were studied by a field emission scanning electron microscope (FESEM) equipped with Energy-dispersive X-ray spectrophotometer (EDS) (MIRA XMU/TESCAN). The powders were suspended in distilled water and treated ultrasonically and then a laser interferometer (Horiba, LB-550) was used to measure the particle size distribution of the milled powder. X-ray powder diffraction patterns (X'Pert. P W 3040/60 Philips, Cu-k_α radiation) in the range of 10–90° (2θ) were collected in order to determine the phase composition of the samples [11]. The crystallite size and residual strain were calculated from the line broadening of XRD reflections by Williamson-Hall equation [11]. The amount of amorphous phases was measured by Eq. (2)Eq. (1) [48]:

$$A = \left(1 - \frac{I}{I_0}\right) \times 100 \quad (1)$$

where, I and I_0 are the intensities of the strongest XRD lines after and before activation respectively.

Nature of chemical bonds was determined by Fourier Transform Infra Red (FTIR, model Nicolet 800). FTIR spectroscopy was employed on both starting mixtures and activated powders (suspended in KBr pellets) at frequency range of 400 to 4000 $Cm^{-1}cm^{-1}$. To reveal more information about the particle morphology of milled powders, we employed a high-resolution transmission electron microscopy (HRTEM: Philips CM 30, Netherlands) technique.

For microstructure studying of the samples by FESEM, all samples were polished using 300 up to 1500 SiC grit and then followed by standard diamond polishing. The micrographs were recorded in back scattered electron mode (BSE). Density of specimens was measured by Archimedes method. Vickers hardness of the samples was measured by applying a load of 10 kg (HV 10) for 15 s (Instron Wolpert, MX-96604) [49]. Toughness measurements were performed by measuring the dimensions of the cracks effect by indenture (by SEM secondary electron mode or optical microscopy) employing Anstis and Nihara method [11,20,50]. Wear tests were carried out by a ball–on-disk test (ASTM G-99-04) [51] in which a ball bearing steel pin (with 5 mm diameter) slides against the specimens. Other typical conditions of: wear load, 2000 gF; sliding speed, 0.2 m s^{-1}; temperature, 25 °C and relative humidity, 24% were employed. The friction coefficient was measured for sliding distance of 720 m (3600 s). The friction force was measured by a machine built–in-cell and the signals delivered from the load cell were changed to the friction coefficients by a personal computer.

3. Results and discussion

3.1. Phase composition and microstructure of the powders

X-ray diffraction patterns of the precursor mixtures and the milled powders (SBN0, SBN50 and SBN100) are presented in Fig. 1. XRD data showed that as a result of increase in the milling time; the intensity of the X-ray reflections in SBN0 powder is reduced and curvature of the XRD background is increased. Thus, the mechanochemical treatment did not produce new phases but the curvature of X-ray background demonstrated the formation of an amorphous phase which resulted from milling. The reflections of AlN by mechanochemical activation were broadened and their intensity were

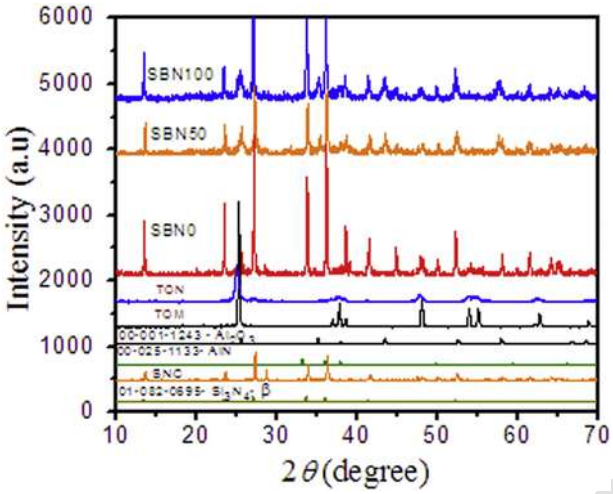

Fig. 1. XRD diffractograms of precursor mixture and milled powders before (SBN0) and after (SBN50 and SBN100) mechanical alloying, "for comparison Si_3N_4, SNC, AlN, Al_2O_3, TOM and TON phases were denoted".

reduced when compared to those precursors. β-Si_3N_4 (acronyms to SNC), TiO_2 (acronyms to TOM (submicron) and TON (nano-size)) coexistence in XRD reflections of milled powders (Fig. 1) illustrated more durability of these phases against activation when compared to AlN.

The curvature of XRD patterns resulted from structural crystal defects such as dislocations, plastic deformation and point defects. Furthermore, unit cell volume of the silicon nitride increased by increasing the milling time. Such changes in lattice parameters are attributed to the aforementioned structural defect [10,52]. The amount of amorphous phase (based on Eq. (1)) in SB100, SBM100 and SBN100 powders measured > 10%. By sintering at temperatures as low as 1500 °C, this amorphous phase will be transformed to a transient liquid phase, thereby, facilitating the sintering of SiAlON/TiN nanocomposites. Additionally, during the liquid phase sintering, activation occurred through Al-active bonds at lower temperatures [20,52]. One may notice that, the decrease in the crystallite size and development of residual strain induced by mechanical alloying, were responsible for broadening of XRD reflections. After 10 h activation, in comparison to un-milled powder, > 40% reduction in crystallite size was determined by Williamson-Hall equation. Furthermore, the residual strain of SB100, SBM100 and SBN100 were increased by approximately 100%. It could be implied that; the freedom of elastic energy and formation of structural defects were responsible for these changes [10,20,27]. Additionally, XRD reflections revealed that TiO_2 (anatase) nanoparticles have been converted to TiN which signified that nitridation of some meta stable TiO_2 powders have been completed [53]. Conversely, the rapid crystallization of TiO_2 amorphous phases in milled powders has occurred.

TEM images for SB100, SBM100 and SBN100 powders are presented in Fig. 2. The TEM images revealed that the milled powders were composed of an amorphous structure with several Si_3N_4 nanocrystalline embedded in them [45,46,53]. In addition, the TEM images showed more particles with dimensions of < 100 nm.

Fig. 3 illustrates the FESEM micrographs of initial (SBM0) and 10 h milled (SBM100) powders. FESEM images demonstrated that the homogenous distribution and non-angular–shapes of particles versus milling time increased. Furthermore, EDS results of milled and un-milled powders indicate that oxygen content of the powder increased by milling and as a consequence resulted in the formation of AlO_4 or Si—O—Al bonds which were required for the formation of SiAlON during sintering [27]. Moreover, such oxidation strongly affects AlN particles and it modifies the microstructure changes [27,52]. In addition, measurement of the particle sizes by FESEM (Fig. 3 right hand pictures) is shown, and it is further confirmed by laser interferometer that the average particle size of the SB100, SBM100 and SBN100 powders were about 120, 155 and 98 nm respectively.

Tracking of the active FTIR intermolecular vibration modes of un-milled (SB0, SBM0 and SBN0) and 10 h milled (SB100, SBM100 and SBN100) powders are shown in Fig. 4. Structural disorder of the β-Si3N4 network caused by mechanical alloying resulted in shifting and broadening of the bonds. Moreover, bonds were shifted and broadened as a result of increase of the structural disorder of the β-Si_3N_4 network. On the contrary, decreasing the degree of structural order caused broadening and decrease in wave number (shifting of wave number) [54]. Bonds in the range of 600–800 $Cmcm^{-1-1}$ (specially the peak at 735 $Cm^{-1}cm^{-1}$) were evidence of dissolving of Al_2O_3 in Si_3N_4 or replacement of Si—N bond with Al—N and Al—O bonds. Furthermore, bonds between 500 and 750 $Cm^{-1}cm^{-1}$ (specially the peak at 510 $Cm^{-1}cm^{-1}$) were evidence of (Al—N), (Al—O, Al—N) and Si_2ON_2 bonds [55]. Existence of β-Si_3N_4 was confirmed by the peaks in the range of 930–1050 $Cm^{-1}cm^{-1}$. Therefore, the FTIR spectra results showed that the components of powders are relatively affected by mechanical alloying and the milled samples enter into aluminosilicate or oxynitride environments. Moreover, the complex absorption in the region of 1400–2000 $Cm^{-1}cm^{-1}$ was evidence of better resolution in crystalline Si_2ON_2 and probably caused by overtone or combination modes of the bulk vibrations [56]. Finally, the upward and downward shifts (small for SB100 and large (due to added TiO_2 precursor) for SBM100 and SBN100) around 3400 $Cm^{-1}cm^{-1}$ originated from amorphous phases [54–56].

3.2. Densification behavior of samples

According to the results of the first section, specimens (from 10 h milled powders) were pressed and sintered at 1750 °C. The X-ray diffraction patterns of PLS and SPS sintered samples are shown in Fig. 5. XRD data of sintered samples indicated that crystallization of amorphous phases in 10 h milled powders has occurred. Moreover, XRD analysis revealed that SBpls75, SBMpls75 and SBNpls75 were poly-phase materials consisting of β-SiAlON as the main phase. Fur-

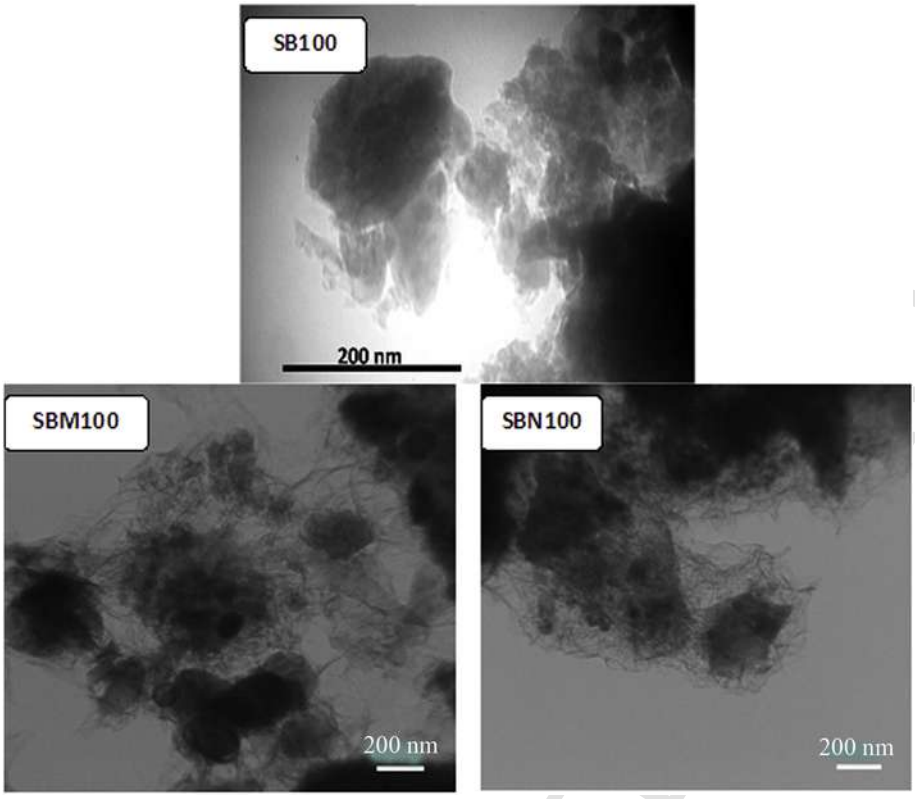

Fig. 2. Transmission electron microscopy images for milled SB100, SBM100 and SBN100 powders.

thermore, the existence of β-SiAlON phase was confirmed by shifting maxima XRD peaks of β-Si_3N_4 towards the left hand [23]. In addition, the overall composition of β-SiAlON in PLS sintered samples was $Si_4Al_2O_2N_6$ (Z = 2) with some O-SiAlON and X-SiAlON. The minor phases such as; O-SiAlON and X-SiAlON can be due to an increase in time or temperature of sintering process. Results revealed that TiN is obtained with major phases in SBMpls and SBNpls samples. Moreover, the most obtained phases of β-SiAlON phase after SPS sintering at 1750 °C was $Si_4Al_2O_2N_6$ (Z = 2) with some X-SiAlON and O-SiAlON. Moreover, like PLS sintered products, TiN has been formed in SBMsps75 and SBNsps75 samples. Existence of β-SiAlON at 1750 °C (sintering temperature) was due to the mechanical alloying activation of the powders, which had a good tendency to transform to β-SiAlON. Thus, one may note that the modified sintering temperature (based on our previous research regarding the present compositions) has been selected. In addition, β-Si_3N_4 was not found in the phase composition and during sintering it changed to β-SiAlON [38,57–59]. The minor meta stable phases such as X-SiAlON ($Si_3Al_6O_{12}N_2$) and O-SiAlON ($Si_6Al_{10}O_{21}N_4$) would be transformed to β-SiAlON during the sintering at higher temperature or post-heat treatment [47]. Moreover, these phases were presented based on SiAlON behavior diagram at 1750 °C (Fig. 6).

The mechanism for obtaining β-SiAlON could be written as follows. By increasing the temperature; silicon nitride eventually reacted with alumina and aluminum nitride, therefore, β-SiAlON has been formed based on Eq. (2) [6,7,60,61].

$$(6-z)/3Si_3N_4 + z/3Al_2O_3 + z/3AlN \rightarrow Si_{6-z}Al_zO_zN_{8-z} \quad (0 \le z \le 4.2) \tag{2}$$

The non-equilibrium condition of the experiments caused z = 2 observation in comparison with the equilibrium condition in the calculation of z value (z = 1.5) [25]. The mechanism for reaching X-SiAlON and O-SiAlON can be written as follows. The silicon nitride reacted with oxygen (which, was produced by reaction of Si_3N_4 with alumina and Alan, in addition, due to excess amount of oxygen after milling) and silica (SiO_2) was formed on the surfaces of Si_3N_4 particles [45,46]. Below the 1200 °C, silica and alumina have partial reaction with each other. Above 1200 °C, silicon nitride eventually reacted with alumina and silica, as a result, X-SiAlON and O-SiAlON were formed [27,52,60,61]. Additionally, O-SiAlON was formed based on Eq. (3) [60,61]:

$$\frac{(2-X)}{4}Si_3N_4 + \frac{X}{2}Al_2O_3 + \frac{(2-X)}{4}SiO_2 \rightarrow Si_{2-X}Al_XO_{1+X}N_{2-X} \quad (0 \le x \le 0.4O-SiAlON) \tag{3}$$

Nevertheless, one may note that, similar phases by SPS and PLS sintering at 1750 °C have been obtained, differing only with the time

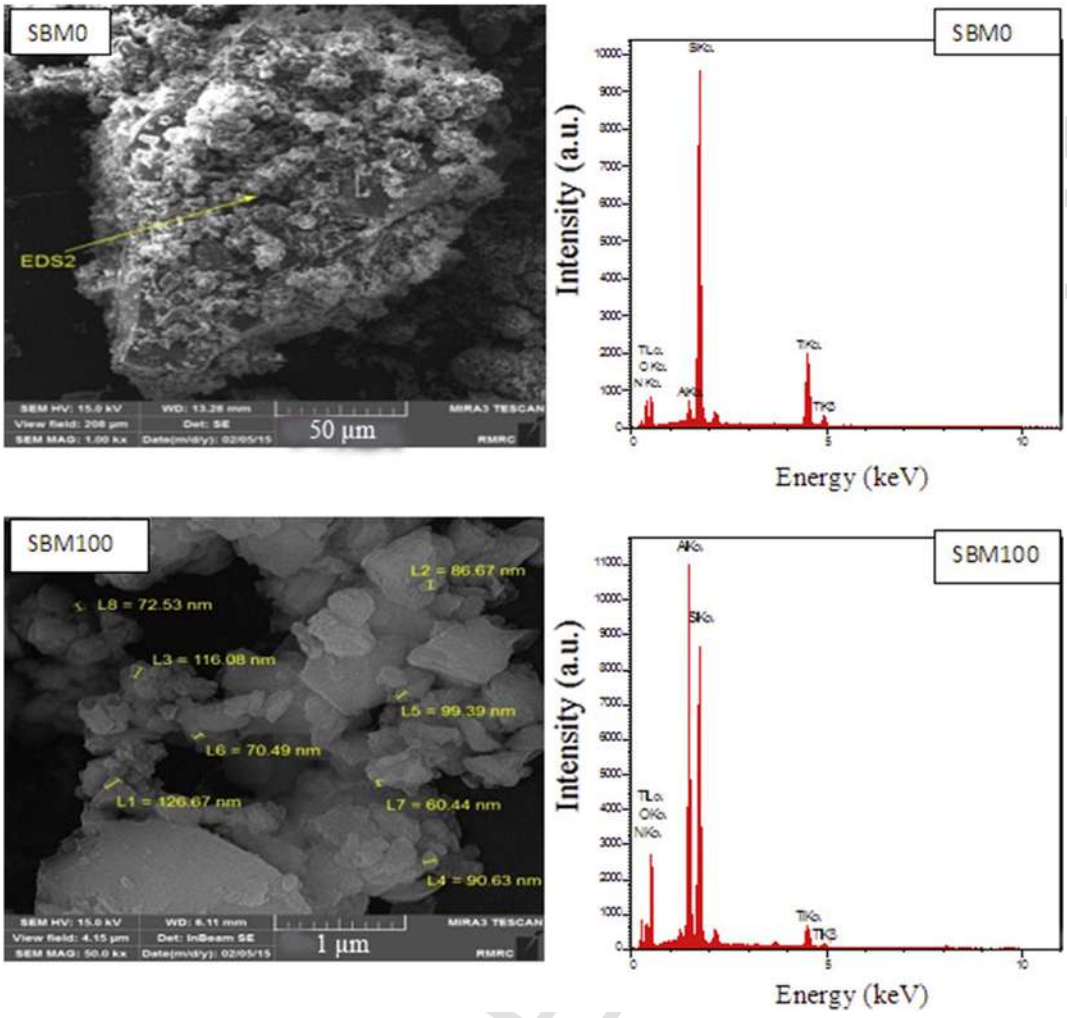

Fig. 3. FESEM micrographs and EDS analysis of un-milled (SBM0) and milled (SBM100) powders.

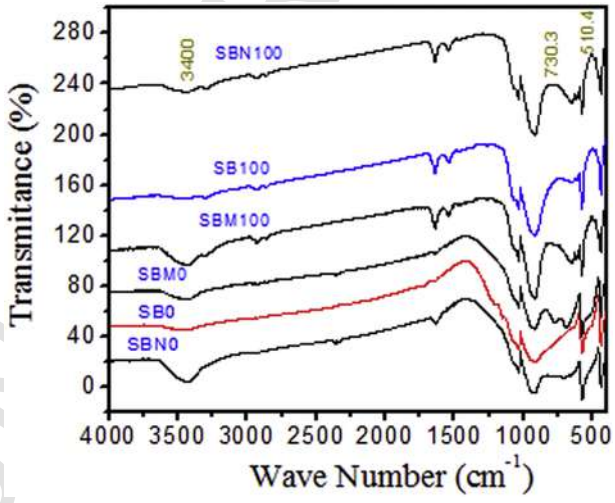

Fig. 4. FTIR spectra (transmittance) for mechanical milled (SB100, SBM100 and SBN100) and un-milled (SB0, SBMo and SBN0) powders.

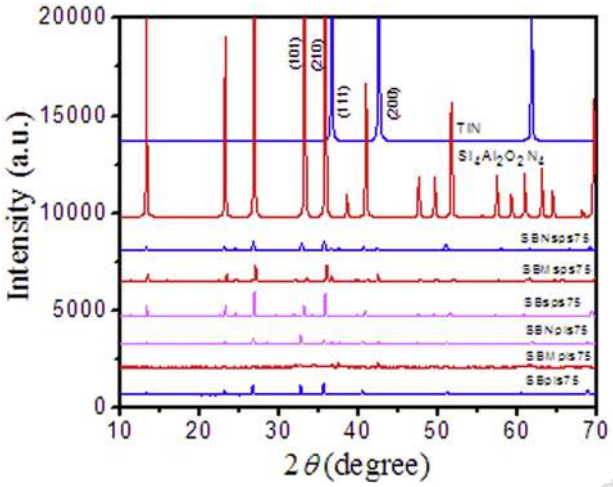

Fig. 5. XRD diffractograms of specimens after PLS sintering at 1750 °C (SBpls75, SBMpls75and SBNpls75) and spark plasma sintering at 1750 °C (SBsps75, SBMsps75 and SBNsps 75), "for comparison of the peaks, TiN and $Si_4Al_2O_2N_6$ phases were denoted." In addition, un-marked peaks are O-SiAlON and X-SiAlON.

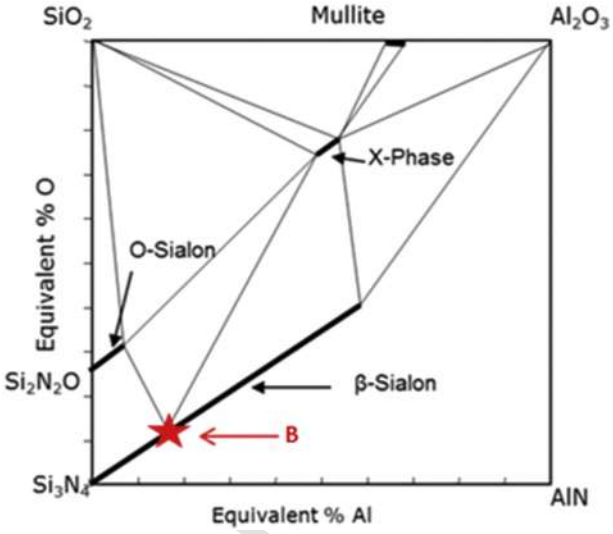

Fig. 6. SiAlON behavior diagram at 1750 °C, starting composition (z = 1.5) was showed with B [39].

of treatment (Fig. 7): by the PLS method, the sintering was completed in 270 min, but by SPS process the samples were obtained within 72 min. Furthermore, changes in phases like from β-Si_3N_4 to α-Si_3N_4 were hindered by the fast cooling rate of SPS process [12].

TiO_2 reacted with silicon nitride and produced TiN, in addition, it lowered the temperature of obtaining SiAlON/TiN composite. The formation reactions of TiN can be written as Eq. (4) [37,45,46,61–66]:

$$1/3Si_3N_4 + TiO_2 \rightarrow SiO_2 + TiN + 1/6N_2 \quad (4)$$

Kurama reported [3] that the abovementioned reactions could occur under reducing conditions or at temperatures above 1350 °C [67]. Thus, selection of the sintering temperature sufficiently above this temperature motivated reactions (2)–(4).

More detailed micrographs of the surfaces of the β-SiAlON/TiN nanocomposites sintered at 1750 °C based on FESEM are presented in Fig. 8. The micrographs on the back scattered mode showed that the microstructure of PLS-ed nanocomposites, possess more porosity and low densification (Fig. 8, left hand pictures). However, there were no obvious pores on the surfaces of polished surfaces of SPS-ed samples, which confirmed full densification of SPS-ed SiAlON/TiN composites (Fig. 8, right hand pictures) [15]. Additionally, large amount of liquid phase and much finer particles of milled samples have triggered particle rearrangement at lower temperature (1750 °C) with a higher shrinkage rate, which utilized full density in SPS-ed samples [68]. Due to the use of Al_2O_3, AlN and TiO_2 as a sintering aid, the grain boundary phases that remained after sintering in the materials have clearly been seen in SPS-ed samples. EDS analyses of SBNsps75 (point A and point B in Fig. 8) indicated that the highest amount of nitrogen (29 at.% N, 22 at.% O, 13 at.% Al and 34 at.% Si) was in section A and the lowest amount of nitrogen (13 at.% N, 42 at.% O, 28 at.% Al and 16 at.% Si) was in grain boundary region or section B. Moreover, secondary chemical compositions occurred with high concentration at grain boundary, which resulted in the attainment of softening of samples at high temperature [67]. Moreover, this glassy phase decreased the strength of bulk ceramics like SiAlON/TiN. However, increase in thermal shock resistance and toughness would occur due to the existence of such phase [67].

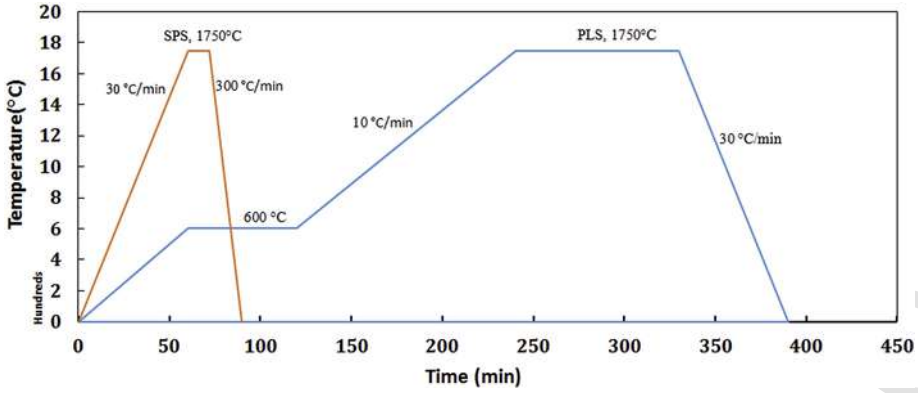

Fig. 7. Comparison of typical sintering cycle of specimens at pressureless and spark plasma sintering.

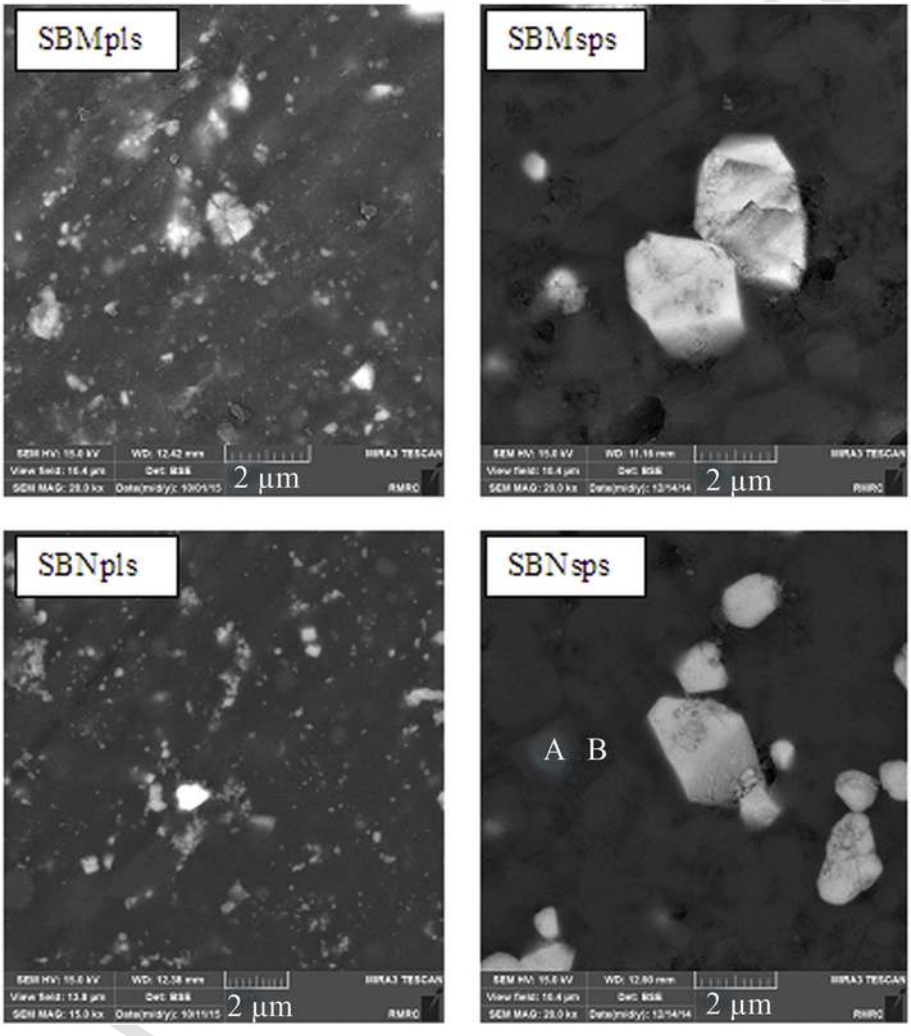

Fig. 8. FESEM micrographs of PLS-ed (SBMpls and SBNpls) and SPS-ed (SBMsps and SBNsps) samples at 1750 °C.

FESEM results confirmed the coexistence of lighter (gray) SiAlON and heavier (white) TiN phases in backscattered images (Fig. 8). These results, verified the homogeneity distribution of TiN particles in the matrix [15]. Due to the large particle sizes of TiN in SBM-sps75 the toughness would be increased [69]. Furthermore, Angu-lar–shaped β-Si_3N_4 grains were not left in the β-SiAlON matrix at 1750 °C. Moreover, cracks caused by the volume change due to the phase transformation of SiAlON were not in [70].

Due to residual micro-porosity observed by FESEM (Fig. 8), PLS-ed specimens could not be considered as fully dense (Table 2). Because of the existence of Al_2O_3, AlN and TiO_2, densification of the samples after the occurrence of liquid phase sintering, was related to

Table 2
Comparison of mechanical properties of samples.

Row	Hardness (HV10) (GPa)	Fracture toughness ($MPa{\cdot}m^{1/2}$)	Friction coefficient	Wear rate ($g{\cdot}m^{-1}$)	Relative density
SBpls	12.9 ± 0.9	4.2 ± 0.6	0.75	1.65E − 05	92%
SBMpls	16.6 ± 0.9	3.4 ± 0.6	0.62	1.25E − 05	92%
SBNpls	14.8 ± 0.9	3.6 ± 0.6	0.69	1.52E − 05	92%
SBsps	14.1 ± 0.5	4.8 ± 0.3	0.6	1.11E − 06	100%
SBMsps	14.6 ± 0.5	6.3 ± 0.3	0.6	3.05E − 06	100%
SBNsps	15.7 ± 0.5	4.0 ± 0.3	0.6	4.72E − 06	100%

the effect of rearrangement of particles and/or softening of the amorphous phase [52].

Hardness and fracture toughness measurements were done by measuring at least 5 indent effects and the averages of measurements were reported in Table 2. The observed differences in indent effects resulted in differences in fracture toughness and hardness of different samples. For instance, the medium diameter of indenture effect in SBMpls and SBMsps was around 105 and 112 μm, respectively, thus, resulting in high hardness in SBMpls sample. Furthermore, due to the low crack propagation in SBMsps, it had gotten higher fracture toughness.

Hardness values of SiAlON and SiAlON-TiN ceramics were reported between ~ 13 GPa and ~ 15.6 GPa, respectively [22,27,71]. With the decrease of TiO_2 particle size from micron to nano-size, the hardness increased from ~ 14.6 to ~ 15.7 GPa in SPS-ed samples. However, in PLS-ed samples caused decrease in hardness from ~ 16.6 (in SBMpls) to ~ 14.8 (in SBNpls). The hardness values in the multiphase samples were depended on the intrinsic hardness of constituents. Moreover, warring in hardness results can be caused by TiN phases that have no homogeneity distribution in the samples. Furthermore, due to the higher hardness of TiN constituents, the hardness values in PLS-ed or SPS-ed nanocomposites were increased in comparison with sintered SiAlONs (SBpls and SBsps samples). On the other hand, coexistence of higher fraction of β-SiAlON and inter granular phases in PLS-ed and SPS-ed samples (such as, SBpls and SBsps) resulted in their lower hardness [22]. It is evident that, TiO_2 powders first particle sizes and different sintering techniques caused different final grain sizes of TiN in samples. The TiN grain size in SPS-ed and PLS-ed samples was below 0.2 and 0.1 μm, respectively (Fig. 8). As a result, increased TiN grain size, led to decrease in hardness from SBNsps to SBMsps. One may note that, incorporation of none homogeneity distribution of phases and relative density of 92% caused more error bars in the results of PLS-ed samples. Moreover, mechanical properties were closely related to the residual porosity of non-full density PLS-ed materials [20,27,38]. Furthermore, in large particle sizes of TiN, the toughness increment occurred in SBMsps75 [69,72].

Lee et al. [15] made Si_3N_4/10 wt.% TiN nanocomposites with full density by SPS technique and obtain nanocomposite with the highest toughness of ~ 4.9 $MPa{\cdot}m^{1/2}$. To reach a relative density of 96% for Si_3N_4–10 wt.% TiN composite, they employed sintering at 1700 °C. Moreover, C. Tian [71] sintered Si_3N_4/10 wt.% TiN nanocomposites with toughness of ~ 6.7 $MPa{\cdot}m^{1/2}$ by HP. H. Mandal et al. [22] have fabricated β-SiAlON ceramic with toughness of ~ 5.6 $MPa{\cdot}m^{1/2}$ by GPS.

With increase in TiO_2 particle size, increase in fracture toughness occurred. Besides, sample without TiO_2 additive had a fracture toughness of ~ 4.2 $MPa{\cdot}m^{1/2}$ (PLS-ed) and ~ 4.8 $MPa{\cdot}m^{1/2}$ (SPS-ed), nevertheless with the addition of 15 wt.% TiO_2, fracture toughness in SPS-ed samples increased to ~ 6.3 $MPa{\cdot}m^{1/2}$. Furthermore, large TiN agglomerates with residual porosity of non-full density PLS-ed materials, might act as defect regions in the PLS-ed composite and caused more decrease in their toughness [73]. On the other hand, good fracture toughness of SBpls and SBNsps (near 4 $MPa{\cdot}m^{1/2}$) in comparison with SBMpls and SBNpls, could be caused by the presence of more elongated β-SiAlON grains in their microstructure [74]. In the SBMsps composite, the fracture toughness reached a value of 6.3 $MPa{\cdot}m^{1/2}$. As a result of the presence of elongated β-SiAlON and TiN phase in the full dense SPS-ed SiAlON-TiN composites, the crack path increment could be the dominant mechanism responsible for toughening. Good densification in the presence of elongated β-SiAlON grains and the positive effects of TiN grains in crack deflection with its harder native, caused good combination of fracture toughness and hardness in SBMsps [69,73,75]. Thus, the SBMsps nanocomposite was processed by the benefits of high fracture toughness in expense of a little reduction in hardness.

Additionally, the friction coefficient and wear rate through sliding distance of specimens during pin-on-disk test are presented in Table 2. The wear data revealed that, friction coefficient was maxima (0.75) in PLS-ed SiAlON sample and minima (0.6) in SPS-ed samples. Higher friction coefficient and wear rate in PLS-ed samples depended on low density of these specimens [76,77]. However, the high density of SPS-ed specimens resulted in lower friction coefficient and wear rate of these specimens [77].

The coexistence of SiAlON and TiN phases in backscattered images (Fig. 9) is verified by FESEM line scan results of SBMsps75. Additionally, FESEM-EDS line scan analyses of SBNsps75 (top picture in Fig. 10) and SBsps75 (left – down picture in Fig. 10) showed that the highest amount of iron particles moved from steel pin to the surface of specimens. One may identify the different appearance of surfaces (Fig. 10 left - down) and analyses of SBNsps75 (top picture in Fig. 10) satisfied it. In addition, such a change in the surface showed higher region of adhesion. On the other hand, the mechanism of adhesive or micro abrasion wear of rubbed surfaces occurred [77]. The studies on the active toughening mechanisms, based on crack path investigation, in nanocomposites were underway and the results would be published in the nearest future. But, based on FESEM results of SBsps75 samples (Fig. 10 right - down) crack deflection was the first suggestion.

4. Conclusions

As it was noticed above, the combination of mechanical alloying and SPS method was considered effective for attainment of the TiN toughened beta SiAlON nanocomposites via low cost Si_3N_4 powder. In addition, by employing and improving this technique to the PLS-ed samples, possible mass production of β-SiAlON/TiN were expected. Based on the experimental results and the abovementioned discussion the following results were concluded: After milling for 10 h, a nanopowder with homogeneous powder samples over length-scale down to 100 nm was produced. Due to the use of high-energy mechanical milling, the amorphization of the starting powders were promoted. Majority of Si_3N_4 particles were transformed into nano-size and were embedded in the amorphous phase. Moreover, the overall composition of samples in PLS and SPS sintered samples was β-SiAlON ($Si_4Al_2O_2N_6$ (Z = 2)) with some O-SiAlON and X-SiAlON. In addition, it was revealed that cubic TiN phase can be formed by the phase transformation of TiO_2 in relation with other precursors. Additionally, according to FTIR results of milled powders some evidence of aluminosilicate or oxynitride material was available at 730.3 and 510.4 $cm^{-1}cm^{-1}$. It was observed that materials which were sintered by PLS, had lower mechanical

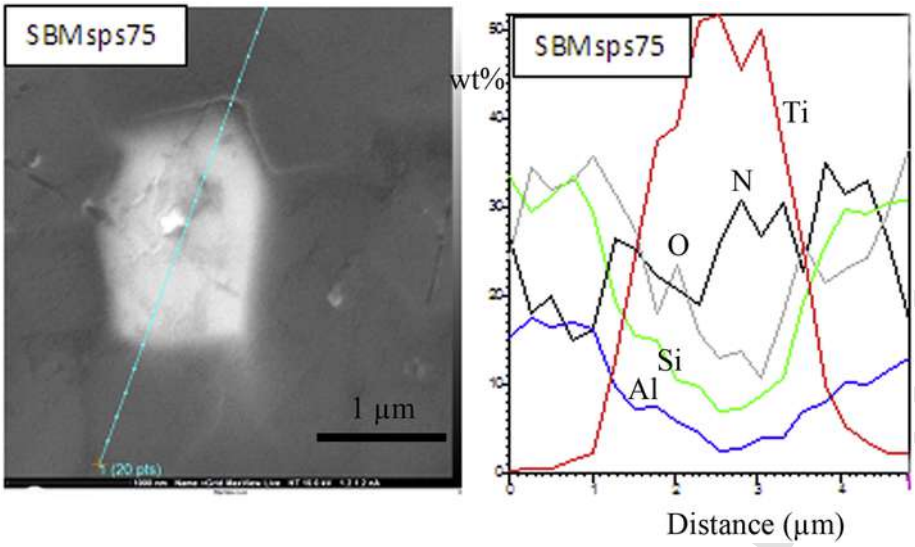

Fig. 9. Line scan graph based on FESEM in SBMsps75.

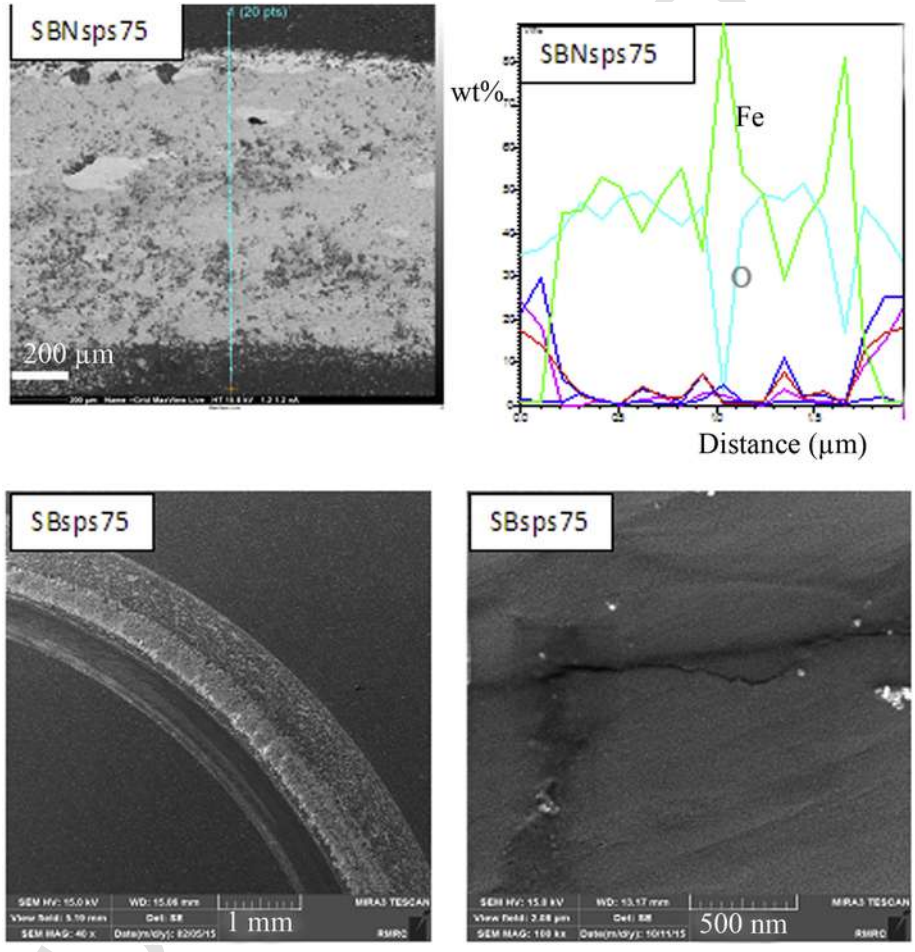

Fig. 10. Wear pass in SBNsps75 (top), wear and crack pass in SBsps75 (down).

properties. However, spark plasma sintering of the β-SiAlON/TiN powder at temperatures as low as 1750 °C resulted in full density ceramics with optimal mechanical properties. Furthermore, β-SiAlON/

TiN SPS sintered samples indicated optimal friction coefficient of 0.6.

References

[1] PENG HP, Spark Plasma Sintering of Si_3N_4-based Ceramics: Sintering Mechanism-Tailoring Microstructure-Evaluating Properties, [Doctoral]. S-10691 Stockholm University, Stockholm, 2004.

[2] G. Tu, S. Wu, J. Liu, Y. Long, B. Wang, Cutting performance and wear mechanisms of Sialon ceramic cutting tools at high speed dry turning of gray cast iron, Int. J. Refract. Met. Hard Mater. 54 (2016) 330–334.

[3] A. Çelik, I. Lazoglu, A. Kara, F. Kara, Investigation on the performance of SiAlON ceramic drills on aerospace grade CFRP composites, J. Mater. Process. Technol. 223 (2015) 39–47.

[4] X. Yi, T. Akiyama, K. Kurokawa, Combustion synthesis and spark plasma sintering of b-SiAlON, in: G. AA, C. LN (Eds.), Nitride Ceramics: Combustion Synthesis, Properties, and Applications, Wiley-VCH Verlag GmbH & Co., Weinheim, Germany, 2015, p. 358. Germany ed. KGaA, Boschstr. 12, 69469.

[5] R. NG, Rare-Earth Doped (Alpha/Beta)-Sialon, University of Warwick institutional repository: University of Warwick, 2001.

[6] S. Kurama, The effects of processing on the α ↔ β SiAlON transformation during cycling heat treatments, Mater. Sci. Eng. A 487 (2008) 278–288.

[7] A. Kheirandish, K.A. Nekouee, R. Khosroshahi, N. Ehsani, Self-propagating high temperature synthesis of SiAlON, Int. J. Refract. Met. Hard Mater. 55 (2016) 68–79.

[8] C. Alexandra, G. Pereira, Development of Sialons Colloidally Processed in Aqueous Medium, Universidade de Aveiro, 2009.

[9] T. Ekstrom, M. Nygren, SiAlON ceramics, J. Am. Ceram. Soc. 75 (1992) 18.

[10] K.J. MacKenzie, J. Temuujin, M.E. Smith, K. Okada, Y. Kameshima, Mechanochemical processing of sialon compositions, J. Eur. Ceram. Soc. 23 (2003) 1069–1082.

[11] P. Pettersson, Z. Shen, M. Johnsson, M. Nygren, Thermal shock resistance of α/β-sialon ceramic composites, J. Eur. Ceram. Soc. 21 (2001) 999–1005.

[12] S. Kurama, I. Schulz, M. Herrmann, Wear properties of α-and α/β-SiAlON ceramics obtained by gas pressure sintering and spark plasma sintering, J. Eur. Ceram. Soc. 31 (2011) 921–930.

[13] T. Ekström, M. Nygren, SiAION ceramics, J. Am. Ceram. Soc. 75 (1992) 259–276.

[14] M. Mitomo, Y. Tajima, Sintering, properties and applications of silicon nitride and sialon ceramics, Nippon Seram. Kyo. Gak 99 (1991) 1014–1025.

[15] C.-H. Lee, H.-H. Lu, C.-A. Wang, P.K. Nayak, J.-L. Huang, Microstructure and mechanical properties of TiN/Si_3N_4 nanocomposites by spark plasma sintering (SPS), J. Alloys Compd. 508 (2010) 540–545.

[16] S. Xiaofei, C. Zhixin, H. Chao, W. Jianjun, L. Xiaodong, R. Hongqiang, et al., Properties of cBN/SiAlON ceramic composites prepared at different sintering temperatures, Rare Metal Mater. Eng. 44 (2015) 196–199.

[17] A. Kandemir, C. Sevik, H. Yurdakul, S. Turan, First-principles investigation of titanium doping into β-SiAlON crystal in TiN–SiAlON composites for EDM applications, Mater. Chem. Phys. 162 (2015) 781–786.

[18] X. Yang, B. Li, C. Zhang, S. Wang, K. Liu, C. Zou, Design and fabrication of porous Si_3N_4—Si_2N_2O in situ composite ceramics with improved toughness, Mater. Des. 110 (2016) 375–381.

[19] C. Zou, B. Li, S. Wang, C. Zhang, Y. Song, Z. Xie, et al., Fabrication and high-temperature mechanical properties of 2.5DSi_3N_{4f}/BN fiber-reinforced ceramic matrix composite, Mater. Des. 92 (2016) 335–344.

[20] O. Eser, S. Kurama, The effect of the wet-milling process on sintering temperature and the amount of additive of SiAlON ceramics, Ceram. Int. 36 (2010) 1283–1288.

[21] M. Herrmann, S. Höhn, A. Bales, Kinetics of rare earth incorporation and its role in densification and microstructure formation of α-Sialon, J. Eur. Ceram. Soc. 32 (2012) 1313–1319.

[22] H. Mandal, N.C. Acikbas, Processing, characterization and mechanical properties of SiAlONs produced from low cost β-Si_3N_4 powder, KONA Powder Particle J. 30 (2013) 22–30.

[23] I. Zalite, N. Zilinska, I. Steins, J. Krastins, Spark Plasma Sintering of SiAlON Nanopowders, IOP Conference Series: Materials Science and Engineering, IOP Publishing, 2011012022.

[24] P. Miranzo, J. González-Julián, M.I. Osendi, M. Belmonte, Enhanced particle rearrangement during liquid phase spark plasma sintering of silicon nitride-based ceramics, Ceram. Int. 37 (2011) 159–166.

[25] X. Yi, K. Watanabe, T. Akiyama, Fabrication of dense β-SiAlON by a combination of combustion synthesis (CS) and spark plasma sintering (SPS), Intermetallics 18 (2010) 536–541.

[26] P. Pettersson, Z. Shen, M. Johnsson, M. Nygren, Thermal shock properties of β-sialon ceramics, J. Eur. Ceram. Soc. 22 (2002) 1357–1365.

[27] M. Sopicka-Lizer, M. Tańcula, T. Włodek, K. Rodak, M. Hüller, V. Kochnev, et al., The effect of mechanical activation on the properties of β-sialon precursors, J. Eur. Ceram. Soc. 28 (2008) 279–288.

[28] N.R. Mojarrad, R. Kheirifard, R.T. Mousavian, Y. Afkham, S. Nakisa, Filling ratio of vial, J. Therm. Anal. Calorim. (2016) 1–7.

[29] M.I. Jones, K. Hirao, H. Hyuga, Y. Yamauchi, S. Kanzaki, Wear properties of Y–α/β composite sialon ceramics, J. Eur. Ceram. Soc. 23 (2003) 1743–1750.

[30] A. Zolriasatein, X. Yan, E. Bauer, P. Rogl, A. Shokuhfar, S. Paschen, Influence of PCA on thermoelectric properties and hardness of nanostructured Ba–Cu–Si clathrates, Mater. Des. 87 (2015) 883–890.

[31] A.F. Boostani, S. Yazdani, R.T. Mousavian, S. Tahamtan, R.A. Khosroshahi, D. Wei, et al., Strengthening mechanisms of graphene sheets in aluminium matrix nanocomposites, Mater. Des. 88 (2015) 983–989.

[32] F. Li, F. Fu, L. Lu, H. Zhang, S. Zhang, Preparation and artificial neural networks analysis of ultrafine β-Sialon powders by microwave-assisted carbothermal reduction nitridation of sol–gel derived powder precursors, Adv. Powder Technol. 26 (2015) 1417–1422.

[33] H. Zhao, P. Wang, J. Yu, J. Zhang, A. Tahmasebi, F. Meng, An experimental study on synthesis of β-Sialon composites using fly ash and lignite char–preparation and whiskers formation, J. Ceram. Soc. Jpn. 123 (2015) 542–549.

[34] J. Souza, C. Santos, C. Kelly, O. Silva, Development of α-SiAlON-SiC ceramic composites by liquid phase sintering, Int. J. Refract. Met. Hard Mater. 25 (2007) 77–81.

[35] H. Ewing, S. Yang, The effect of precursor composition and sintering additives on the formation of β-sialon from Al, Si and Al_2O_3 powders, Ceram. Int. 37 (2011) 1667–1673.

[36] H. Wang, T. Tomiya, T. Takeda, N. Hirosaki, O. Odawara, H. Wada, Fabrication of nanoscale Ca-α-SiAlON:Eu^{2+} phosphor by laser ablation in water, Appl. Phys. Express 8 (2015), 115001.

[37] N. Ahmad, H. Sueyoshi, Properties of Si_3N_4–TiN composites fabricated by spark plasma sintering by using a mixture of Si_3N_4 and Ti powders, Ceram. Int. 36 (2010) 491–496.

[38] O. Eser, S. Kurama, A comparison of sintering techniques using different particle sized β-SiAlON powders, J. Eur. Ceram. Soc. 32 (2012) 1343–1347.

[39] P. Calloch, I.W. Brown, K.J. MacKenzie, J.V. Hanna, G.J. Rees, Synthesis and properties of new β-Sialon/TiN composites via a novel Al_xTi_y intermediate, Ceram. Int. 42 (2016) 2330–2338.

[40] K.A. Nekouee, R. Khosroshahi, R.T. Mousavian, N. Ehsani, Sintering behavior and microwave dielectric properties of SiO_2–MgO–Al_2O_3–TiO_2 ceramics, J. Mater. Sci. Mater. Electron. 27 (2016) 3570–3575.

[41] M.S. Asl, B. Nayebi, Z. Ahmadi, P. Pirmohammadi, M.G. Kakroudi, Fractographical characterization of hot pressed and pressureless sintered SiAlON-doped ZrB_2–SiC composites, Mater. Charact. 102 (2015) 137–145.

[42] Z. Ahmadi, B. Nayebi, M.S. Asl, M.G. Kakroudi, Fractographical characterization of hot pressed and pressureless sintered AlN-doped ZrB_2–SiC composites, Mater. Charact. 110 (2015) 77–85.

[43] D. Demirskyi, Y. Sakka, O. Vasylkiv, High-temperature reactive spark plasma consolidation of TiB_2–NbC ceramic composites, Ceram. Int. 41 (2015) 10828–10834.

[44] J. Niu, X. Yi, K. Harada, T. Akiyama, Spark plasma sintering of α/β-SiAlON synthesized by salt-assisted combustion, J. Alloys Compd. 689 (2016) 266–270.

[45] T.G. Tien, Use of Phase Diagrams in the Study of Silicon Nitride Ceramics, Department of Materials Science and Engineering, University of Michigan, 1995.

[46] K. Krnel, A. Maglica, T. Kosmač, β-SiAlON/TiN nanocomposites prepared from TiO_2-coated Si_3N_4 powder, J. Eur. Ceram. Soc. 28 (2008) 953–957.

[47] H. Mandal, D. Thompson, New heat treatment methods for glass removal from silicon nitride and sialon ceramics, J. Mater. Sci. 35 (2000) 6285–6292.

[48] X. Yi, T. Akiyama, Mechanical-activated, combustion synthesis of β-SiAlON, J. Alloys Compd. 495 (2010) 144–148.

[49] C. Ullner, A. Germak, H. Le Doussal, R. Morrell, T. Reich, W. Vandermeulen, Hardness testing on advanced technical ceramics, J. Eur. Ceram. Soc. 21 (2001) 439–451.

[50] G. Anstis, P. Chantikul, B.R. Lawn, D. Marshall, A critical evaluation of indentation techniques for measuring fracture toughness: I, direct crack measurements, J. Am. Ceram. Soc. 64 (1981) 533–538.

[51] Norma A. G99–04. Standard test method for wear testing with a pin-on-disk apparatus. 2004.

[52] M. Sopicka-Lizer, C. Duran, H. Gocmez, T. Pawlik, M. Mikuskiewicz, K. MacKenzie, Effect of high energy milling on the formation and properties of sialon ceramics prepared from silicon nitride-aluminium nitride precursors, Ceram. Int. 39 (2013) 4269–4279.

[53] L. Gao, J. Li, T. Kusunose, K. Niihara, Preparation and properties of TiN–Si_3N_4 composites, J. Eur. Ceram. Soc. 24 (2004) 381–386.

[54] A. Takase, E. Tani, Hot-pressing temperature dependence of Raman and infrared spectra of sialons, J. Mater. Sci. Lett. 7 (1988) 793–794.

[55] V. Antsiferov, V. Gilyov, V. Karmanov, IR-spectra and phases structure of sialons, Vib. Spectrosc. 30 (2002) 169–173.
[56] G. Busca, V. Lorenzelli, M. Baraton, P. Quintard, R. Marchand, FT-IR characterization of silicon nitride Si_3N_4 and silicon oxynitride Si_2ON_2 surfaces, J. Mol. Struct. 143 (1986) 525–528.
[57] I. Zalite, N. Zilinska, G. Kladler, SiAlON ceramics from nanopowders, J. Eur. Ceram. Soc. 28 (2008) 901–905.
[58] A. Rosenflanz, I. Chen, Kinetics of phase transformations in SiAlON ceramics: II. Reaction paths, J. Eur. Ceram. Soc. 19 (1999) 2337–2348.
[59] N.C. Acikbas, R. Kumar, F. Kara, H. Mandal, B. Basu, Influence of β-Si_3N_4 particle size and heat treatment on microstructural evolution of α:β-SiAlON ceramics, J. Eur. Ceram. Soc. 31 (2011) 629–635.
[60] P. Calloch, New Reaction Paths for Advanced SiAlON/TiN Composites, Victoria University of Wellington, 2015.
[61] A. Roine, HSC Chemistry 6.0, 6 ed, Outokumpu Research Oy, 2006.
[62] Y.F. Kargin, S. Ivicheva, A. Lysenkov, N. Ovsyannikov, L. Shvorneva, K. Solntsev, Si_3N_4/TiN composites produced from TiO_2-modified Si_3N_4 powders, Inorg. Mater. 48 (2012) 897–902.
[63] R.-G. Duan, G. Roebben, J. Vleugels, O. Van der Biest, In situ formation of Si_2N_2O and TiN in Si_3N_4-based ceramic composites, Acta Mater. 53 (2005) 2547–2554.
[64] M. Herrmann, B. Balzer, C. Schubert, W. Hermel, Densification, microstructure and properties of Si_3N_4·Ti (C, N) composites, J. Eur. Ceram. Soc. 12 (1993) 287–296.
[65] M.B. Trigg, K.H. Jack, The fabrication of O′-sialon ceramics by pressureless sintering, J. Mater. Sci. 23 (1988) 481–487.
[66] A. Vučković, S. Bošković, B. Matović, M. Vlajic, V. Krstic, Effect of β-Si_3N_4 seeds on densification and fracture toughness of silicon nitride, Ceram. Int. 32 (2006) 303–307.
[67] D. Richerson, D.W. Richerson, W.E. Lee, Modern Ceramic Engineering: Properties, Processing, and Use in Design, CRC press, 2005.
[68] X. Xu, T. Nishimura, N. Hirosaki, R.J. Xie, H. Tanaka, Fabrication of a Nano-Si_3N_4/Nano-C composite by high-energy ball milling and spark plasma sintering, J. Am. Ceram. Soc. 90 (2007) 1058–1062.
[69] B. Zou, C. Huang, H. Liu, M. Chen, Preparation and characterization of Si_3N_4/TiN nanocomposites ceramic tool materials, J. Mater. Process. Technol. 209 (2009) 4595–4600.
[70] M. Hotta, T. Goto, Effect of time on microstructure and hardness of βSiAlON–cubic boron nitride composites during spark plasma sintering, Ceram. Int. 37 (2011) 521–524.
[71] C. Tian, H. Jiang, N. Liu, Thermal shock behavior of Si_3N_4–TiN nano-composites, Int. J. Refract. Met. Hard Mater. 29 (2011) 14–20.
[72] I. Ahmad, M. Islam, H.S. Abdo, T. Subhani, K.A. Khalil, A.A. Almajid, et al., Toughening mechanisms and mechanical properties of graphene nanosheet-reinforced alumina, Mater. Des. 88 (2015) 1234–1243.
[73] T. Ekström, P.-O. Olsson, ß-Sialon ceramics with TiN particle inclusions, J. Eur. Ceram. Soc. 13 (1994) 551–559.
[74] A.K. Mallik, N.C. Acikbas, F. Kara, H. Mandal, D. Basu, A comparative study of SiAlON ceramics, Ceram. Int. 38 (2012) 5757–5767.
[75] S. Abo-Naf, U. Dulias, J. Schneider, K.-H. Zum Gahr, S. Holzer, M. Hoffmann, Mechanical and tribological properties of Nd-and Yb-SiAlON composites sintered by hot isostatic pressing, J. Mater. Process. Technol. 183 (2007) 264–272.
[76] Z.-H. Xie, M. Hoffman, R. Moon, P. Munroe, Y.-B. Cheng, Sliding wear behaviour of Ca α-sialon ceramics at 600 °C in air, Wear 260 (2006) 1356–1360.
[77] P. Reis, J.P. Davim, X. Xu, J. Ferreira, Tribological behaviour of colloidally processed sialon ceramics sliding against steel under dry conditions, Tribol. Lett. 18 (2005) 295–301.